catalysts

MDPI

Article

Synthesis and Characterization of Mesoporous Silica Nanoparticles Loaded with Pt Catalysts

Xingyi Lyu [1,†], Xun Wu [2,†], Yuzi Liu [3], Wenyu Huang [2,4,*], Byeongdu Lee [5,*] and Tao Li [1,5,*]

1 Department of Chemistry and Biochemistry, Northern Illinois University, DeKalb, IL 60115, USA; Z1909024@students.niu.edu
2 Department of Chemistry, Iowa State University, Ames, IA 50011, USA; xunw@iastate.edu
3 Center for Nanoscale Materials, Argonne National Laboratory, Lemont, IL 60439, USA; yuziliu@anl.gov
4 Ames Laboratory, Ames, IA 50011, USA
5 X-ray Science Division, Argonne National Laboratory, Lemont, IL 60439, USA
* Correspondence: whuang@iastate.edu (W.H.); blee@anl.gov (B.L.); taoli@anl.gov (T.L.)
† The two authors contributed equally.

Abstract: Coating the catalyst with a nanoporous layer has been demonstrated to be an effective approach to improve catalyst stability. Herein, we systematically investigate two types of core-shell mesoporous silica nanoparticles with a platinum nanocatalyst using a variety of characterization methods. One of the mesoporous particles has a unique amine ring structure in the middle of a shell (Ring-mSiO_2/Pt-5.0/SiO_2), and the other one has no ring structure (mSiO_2/Pt-5.0/SiO_2). Brunauer–Emmett–Teller/Barrett–Joyner–Halenda (BET/BJH) presented a similar surface area for both particles, and the pore size was 2.4 nm. Ultra-Small-Angle X-ray Scattering (USAXS)/ Small-Angle X-ray Scattering (SAXS) showed the size of mSiO_2/Pt-5.0/SiO_2 and Ring-mSiO_2/Pt-5.0/SiO_2 were 420 nm and 272 nm, respectively. It also showed that the ring structure was 30 nm above the silica core. Using high-resolution Transmission Electron Microscopy (TEM), it was found that the platinum nanoparticles are loaded evenly on the surface of the silica. In situ SAXS heating experiments and Thermogravimetric Analysis (TGA) indicated that the mSiO_2/Pt-5.0/SiO_2 were more stable during the high temperature, while the Ring-mSiO_2/Pt-5.0/SiO_2 had more change in the particle.

Keywords: mesoporous materials; USXAS/SXAS

Citation: Lyu, X.; Wu, X.; Liu, Y.; Huang, W.; Lee, B.; Li, T. Synthesis and Characterization of Mesoporous Silica Nanoparticles Loaded with Pt Catalysts. *Catalysts* **2022**, *12*, 183. https://doi.org/10.3390/catal12020183

Academic Editors: John Vakros, Evroula Hapeshi, Catia Cannilla and Giuseppe Bonura

Received: 30 December 2021
Accepted: 30 January 2022
Published: 31 January 2022

1. Introduction

Since the past century, plastic has played an essential role in people's daily lives and industry development due to many advantages, such as being economy-friendly, lightweight, and chemical-resistant [1–3]. However, since plastic materials take centuries to degrade, recycling plastic waste is a thorny problem worldwide. Even one piece of plastic waste can cause chemical and physical hazards to wildlife and the environment [4–6], not to mention that 4.8 to 12.7 million tons of plastic waste leak into the ocean every year [7,8]. The United States generates approximately 30 million tons of plastic waste each year, most of which goes to landfills, and less than 10% has been recycled [9]. Currently, the effective recycling of plastic waste and the production of high-value chemicals are research hotspots [10–12]. The use of metal catalysts to degrade waste plastics is a promising approach for plastic recycling because this helps to convert those synthetic polymers into useful liquid fuels or other valuable materials [13–15].

One issue of this recycling is the high temperature required, which will make the nanocatalyst sintered. To address this issue, a series of materials have been introduced. For example, carbon support [16], $SrTiO_3$ perovskite nanocuboid [17–19], atomic layer deposition (ALD) overcoats [20–22], mesoporous silica nanoparticles [23], mesoporous aluminosilica spheres [24], and many other materials have been studied as the support and protective layer to prevent deactivation of the catalysts. Among the above materials,

mesoporous silica nanoparticles are an excellent candidate to stabilize catalysts. Xiao et al. confined Pt nanoparticles inside mesoporous SiO_2 wells and proved their stability [23]. Recently, the Pt NPs have been replaced by intermetallic nanoparticles, which were also stable at high temperatures [25]. Tennakoon et al. also utilized the mesoporous silica nanoparticles to protect Pt NPs from the harsh environment during the process of upcycling high-density polyethylene [26].

Mesoporous silica nanoparticles also have many applications in other fields, such as cancer theranostics [27,28], tissue engineering [29], and contaminated-water treatment [30]. Although much progress has been made to show that mesoporous silica nanoparticles are eligible for many applications, there has not been a thorough study on the characterization of the particles' structure. We began with a model system, named mesoporous silica shell/5 nm Pt nanoparticle/solid silica, ($mSiO_2$/Pt-5.0/SiO_2) structure nanoparticle as reported before [31–33]. For comparison, a new structure with an amine ring added in the shell was first synthesized, which potentially can be functionalized as a spatial-selective site for a single-site catalyst. In addition, we utilized advanced characterization techniques such as Brunauer–Emmett–Teller (BET), Ultra-Small-Angle X-ray Scattering (USAXS)/Small-Angle X-ray Scattering (SAXS), and Transmission Electron Microscopy (TEM) to study these particles' structure. The BET theory and the Barrett–Joyner–Halenda (BJH) model showed that the pore size was 2.4 nm, and the surface area was similar. USAXS/SAXS showed the size of $mSiO_2$/Pt-5.0/SiO_2 and Ring-$mSiO_2$/Pt-5.0/SiO_2 were 420 nm and 272 nm, respectively. It also showed that the ring structure was 30 nm above the silica core. TEM showed that the platinum nanoparticles are loaded evenly on the surface of the silica. The SAXS heating experiment has been deployed to understand thermally induced morphological changes. The changes in particle size and $d_{spacing}$ of Ring-$mSiO_2$/Pt-5.0/SiO_2 are both greater than the changes of $mSiO_2$/Pt-5.0/SiO_2.

2. Results and Discussion

2.1. Synthesis of $mSiO_2$/Pt-5.0/SiO_2 and Ring-$mSiO_2$/Pt-5.0/SiO_2

As shown in Scheme 1, two types of mesoporous structure silica nanoparticles were synthesized. The first one was the core-shell mesoporous silica nanoparticle with Pt nanoparticle ($mSiO_2$/Pt-5.0/SiO_2), while the second was the core-shell mesoporous silica nanoparticle with ring structure (Ring-$mSiO_2$/Pt-5.0/SiO_2). The synthesis methods for both were the same during the first several steps. After those silica spheres were successfully obtained, the Pt NPs were added to the surface with the help of the -NH_2 functional group. The benefit of introducing the -NH_2 was to increase the binding force between the silica and the Pt NPs [23]. The above steps were identical for $mSiO_2$/Pt-5.0/SiO_2 and Ring-$mSiO_2$/Pt-5.0/SiO_2. The processes to grow the mesoporous structure were different. For $mSiO_2$/Pt-5.0/SiO_2, the hexadecyltrimethylammonium bromide (C_{16}TAB) and the tetraethyl orthosilicate (TEOS) were used as the templating agent and the precursor, respectively. For the synthesis of the ring structure, the addition of TEOS was divided into two steps, between which the 3-aminopropyl trimethoxy silane (ATPS) was added to the system to form the ring structure in the shell.

2.2. Surface Area Analysis

Next, it is important to understand the porous structures of these two materials. To investigate the surface area and porosity difference, N_2 adsorption and desorption experiments were performed. Figure 1a shows that both samples show a type IV isotherm based on the International Union of Pure and Applied Chemistry (IUPAC) classification, and all analytical data are presented in the Table 1. No shape difference can be obtained from the isotherm. Then, the Barrett–Joyner–Halenda (BJH) model was used to analyze the mesopore size based on the data between 0.1–0.3 p/p^0. As seen in Figure 1b, both samples have a sharp peak at the pore size of 24 Å. No other peaks were observed in the BJH model. The BET surface area for normal-$mSiO_2$/SiO_2 is 1020 m^2/g, larger than 950 m^2/g for Ring-$mSiO_2$/SiO_2 sample, and pore volume data shows the same trend as

the normal sample has a larger pore volume than ring sample. These two data were also reflected on the isotherm and BJH pore size distribution. Concerning the ring area may have a much narrower pore, nonlocal density function theory (NLDFT) was used to probe the micropore range, as shown in Figure 1c. No apparent difference can be obtained from the comparison based on NLDFT pore size distribution. One thing worth noting is that the negligible difference between these two samples does not mean the two samples are identical in their pore structure. Because the APTS/TEOS ratio is 1:35, the change of the pore may be too small for the instrument to detect but has the potential to impact catalysis.

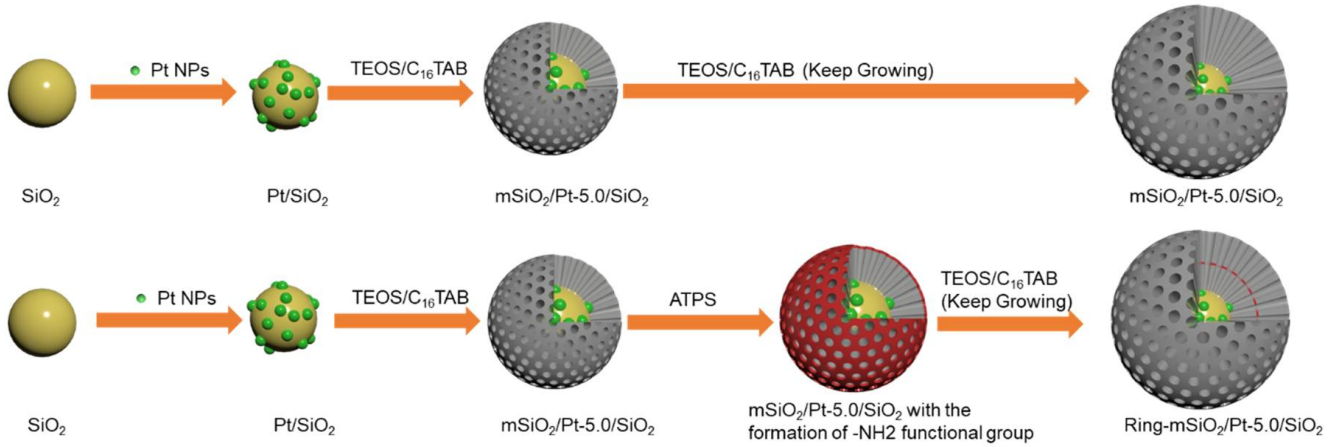

Scheme 1. Preparation of $mSiO_2$/Pt-5.0/SiO_2 and Ring-$mSiO_2$/Pt-5.0/SiO_2.

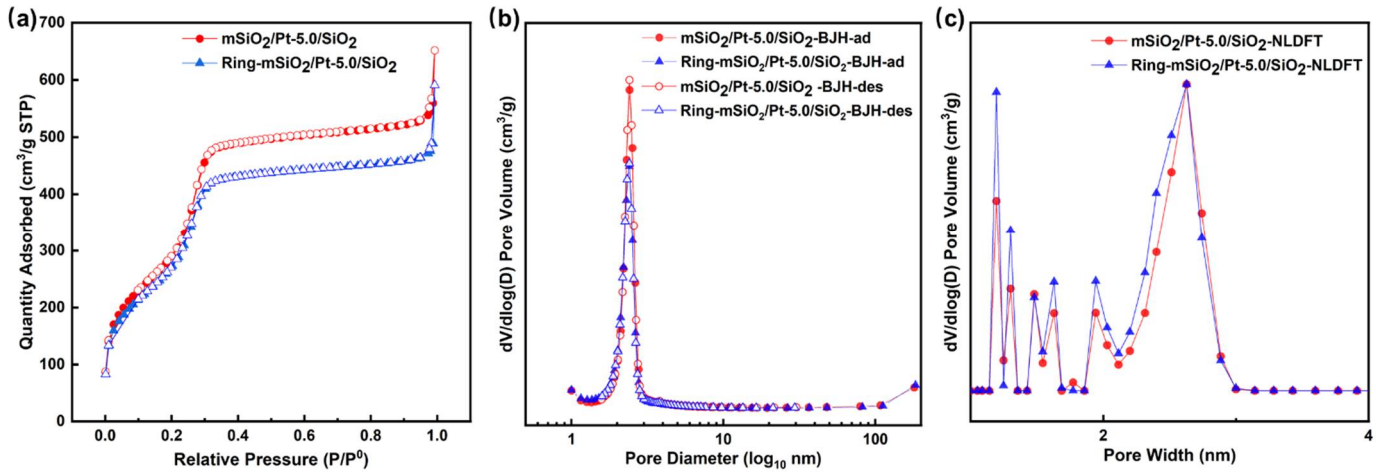

Figure 1. (**a**) Nitrogen adsorption/desorption isotherm curves; (**b**) Pore size distributions from Barrett–Joyner–Halenda (BJH) model; (**c**) Pore size distribution from nonlocal density functional theory (NLDFT) of $mSiO_2$/Pt-5.0/SiO_2 and Ring-$mSiO_2$/Pt-5.0/SiO_2.

Table 1. Average parameters for $mSiO_2$/Pt-5.0/SiO_2 and Ring-$mSiO_2$/Pt-5.0/SiO_2.

	BET Surface Area (m^2/g)	Pore Volume (cm^3/g)	BJH Pore Size-Ads (Å)	BJH Pore Size-Des (Å)
$mSiO_2$/Pt-5.0/SiO_2	1020	0.81	24	24
Ring-$mSiO_2$/Pt-5.0/SiO_2	950	0.71	24	24

2.3. Ultra-Small-Angle X-Ray Scattering (USAXS)/Small-Angle X-Ray Scattering(SAXS)

Furthermore, the USAXS/SAXS measurements were used to obtain structural information such as the shell thickness and the ring position, as shown in Figure 2. SAXS has been demonstrated to be a powerful technique to study porous material [34–37]. The principal

peak positions q_1 at low q region for $mSiO_2$/Pt-5.0/SiO_2 and Ring-$mSiO_2$/Pt-5.0/SiO_2 are 0.169 $Å^{-1}$ and 0.168 $Å^{-1}$, respectively. The pore center-to-center distances ($d_{spacing}$) should be 3.718 nm for both particles, which is calculated from $d_{spacing} = \frac{2\pi}{q_1}$ [38]. By considering the pore size diameter of 2.400 nm from the BET theory, the thickness of the pore's wall is estimated to be 1.300 nm. To know the thickness of the shell, the electron density of silica was calculated and processed based on the USAXS data from Figure 2a and displayed as the function of radius in Figure 2b. The highest electron density at 0.7 $Å^{-3}$ comes from the silica spheres as the core. The clifflike drop in electron density near the radius of 60 nm proved the successful synthesis of 120 nm silica spheres. The peak around 90 nm indicated the position of the ring structure, which is about 30 nm above the silica spheres. The second and third clifflike declines around 136 nm and 210 nm indicate the radius of the entire nanoparticles. Based on that, we know the diameters of $mSiO_2$/Pt-5.0/SiO_2 and Ring-$mSiO_2$/Pt-5.0/SiO_2 are around 420 nm and 272 nm, respectively.

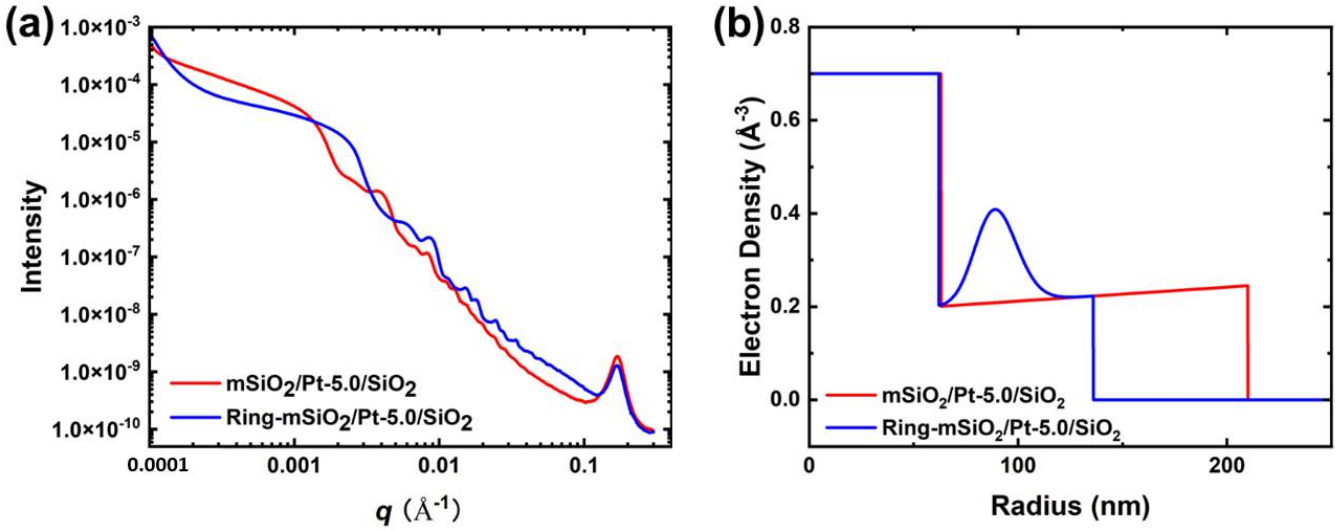

Figure 2. (**a**) 1D Ultra-Small-Angle X-ray Scattering (USAXS) profile and (**b**) electron density of $mSiO_2$/Pt-5.0/SiO_2 and Ring-$mSiO_2$/Pt-5.0/SiO_2.

2.4. Transmission Electron Microscopy (TEM) Characterization

In order to obtain more direct information about the morphology and other structures of these particles, high-resolution TEM images of $mSiO_2$/Pt-5.0/SiO_2 and Ring-$mSiO_2$/Pt-5.0/SiO_2 were taken and shown in Figure 3. Figure 3a–d shows bright-field TEM images and High Angle Annular Dark Field (HAADF) STEM images, respectively. As shown in Figure 3a,b, the large dark spheres in the center are the silica core. The regular striped texture around the core should be the mesoporous shell. These high-magnification images illuminate the Pt NPs located at the bottom of the mesoporous shell, near the surface of the silica spheres as we expected. What is more, the ring structure has been clearly observed in the mesoporous shell. The results in the TEM images provide a valuable and direct perspective about the nanoparticles, which agree well with USAXS/SAXS data.

2.5. In Situ Small-Angle X-Ray Scattering (SAXS) Heating Experiment

After understanding the structure of both samples, the study of thermal stability is the most important because the catalytic process is carried out at high temperatures. Therefore, in situ SAXS heating experiment was deployed for both mesoporous nanoparticles. The results are displayed as a form of color-filled contour line plot. As we can see from Figure 4a, the q_1 position of $mSiO_2$/Pt-5.0/SiO_2 has no significant change with the increase in the temperature, which indicates that the structure of this no-ring nanoparticle is stable. In contrast, in Figure 4b, the q_1 position of Ring-$mSiO_2$/Pt-5.0/SiO_2 shifts to the high q region after 100 °C. This change may indicate the change of structure of Ring-$mSiO_2$/Pt-5.0/SiO_2.

In order to better compare the structure before and after the temperature rise, the 1D SAXS profile for each nanoparticle at 30 °C and 400 °C is shown in Figure 4c,d. As can be observed, q_1 for $mSiO_2$/Pt-5.0/SiO_2 only changed a little from 0.170 $Å^{-1}$ to 0.175 $Å^{-1}$, while q_1 for Ring-$mSiO_2$/Pt-5.0/SiO_2 changed a great deal from 0.169 $Å^{-1}$ to 0.180 $Å^{-1}$. The change of q_1 caused the change of $d_{spacing}$. The continuous change is displayed in Figure 4e. The change of $d_{spacing}$ for Ring-$mSiO_2$/Pt-5.0/SiO_2 is about 0.2 nm, which is about twice the change of $mSiO_2$/Pt-5.0/SiO_2. The changes in relative particle size are also calculated and displayed in Figure 3f. With the temperature going up, the relative size change of Ring-$mSiO_2$/Pt-5.0/SiO_2 is about two times larger than $mSiO_2$/Pt-5.0/SiO_2.

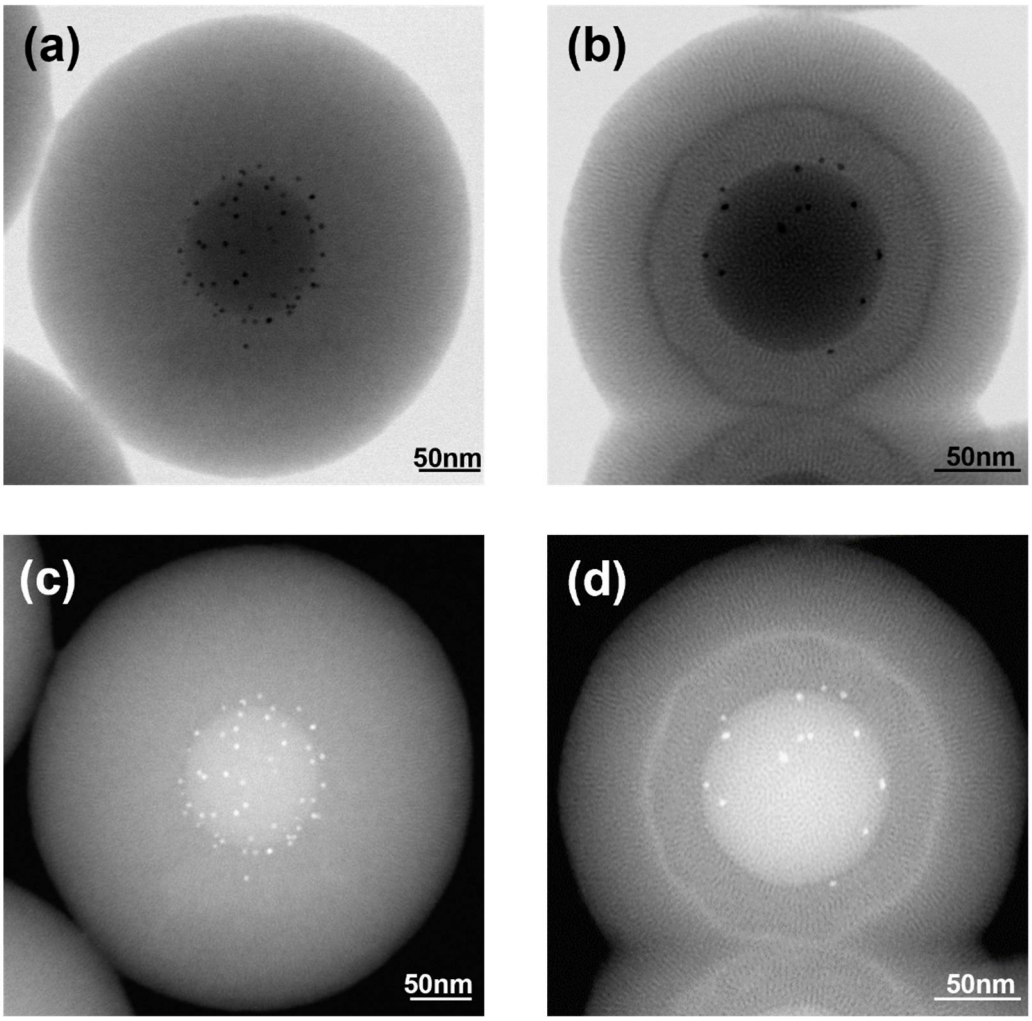

Figure 3. Bright Field Transmission Electron Microscopy (TEM) images for (**a**) $mSiO_2$/Pt-5.0/SiO_2; (**b**) Ring-$mSiO_2$/Pt-5.0/SiO_2; High Angle Annular Dark Field STEM (HAADFSTEM) images for (**c**) $mSiO_2$/Pt-5.0/SiO_2 at scale of 50 nm and (**d**) Ring-$mSiO_2$/Pt-5.0/SiO_2.

2.6. Thermogravimetric Analysis (TGA)

Although in situ SAXS heating experiment clearly shows the different stability for the two particles, it is still unclear about the cause. We used TGA to understand better the pyrolysis processes of $mSiO_2$/Pt-5.0/SiO_2 and Ring-$mSiO_2$/Pt-5.0/SiO_2. The normalized TGA curves are shown in Figure 5. There is no significant difference between both nanoparticles. The relative weight losses were around 12.5%, which means there was not much organic material in the system as we expected. The weight increase at the very beginning comes from the buoyancy effect. The weight loss around 100 °C to 300 °C should be contributed from the desorption of the water and organic solvent residue from the preparation process.

The loss of chemisorbed water and organic solvent may be the reason for weight loss at a higher temperature above 300 °C. Such results are similar to an ALD system [39].

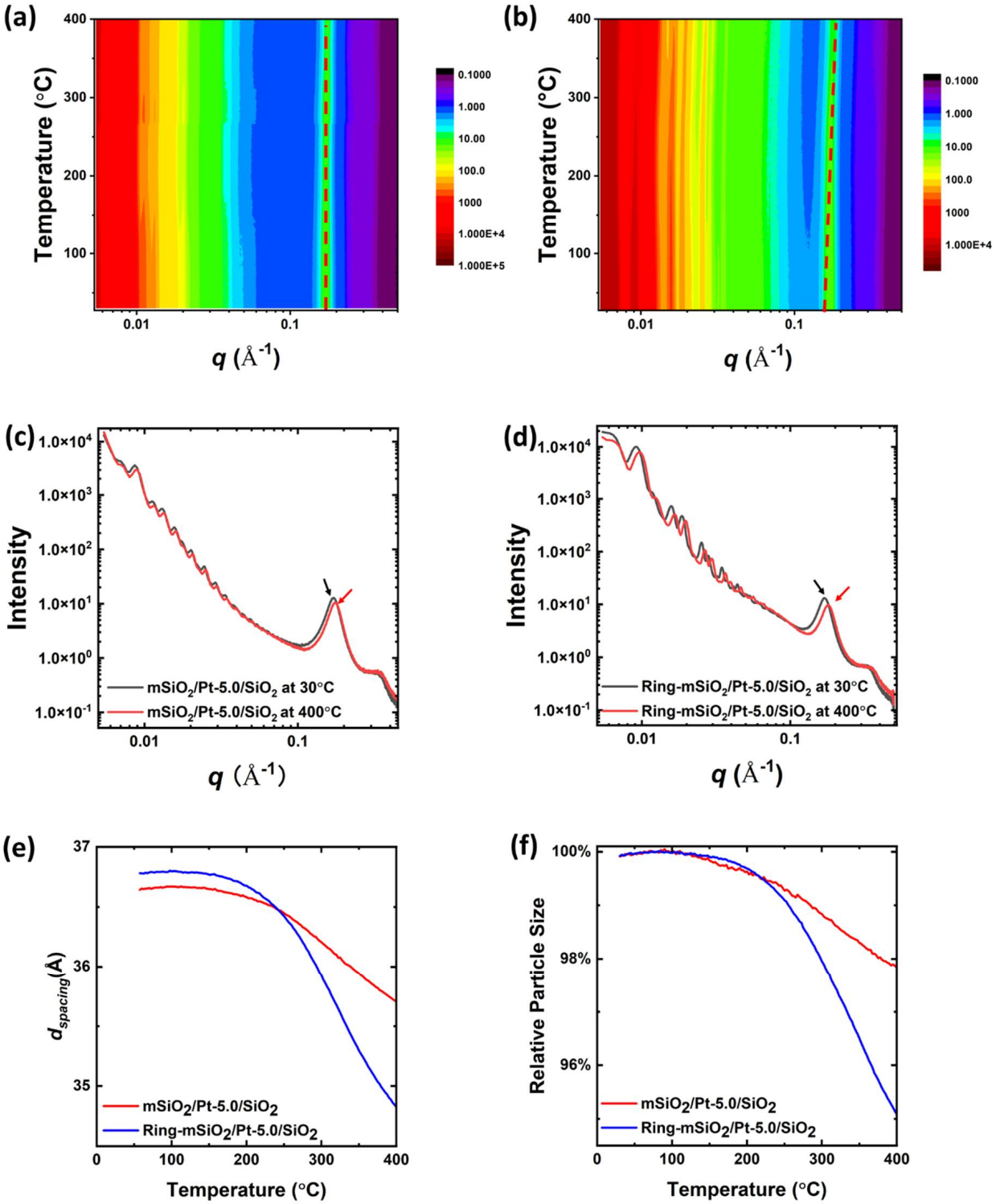

Figure 4. The color-filled contour line plot for (**a**) $mSiO_2/Pt\text{-}5.0/SiO_2$ and (**b**) $Ring\text{-}mSiO_2/Pt\text{-}5.0/SiO_2$.The 1D Small-Angle X-ray Scattering (SAXS) profile for (**c**) $mSiO_2/Pt\text{-}5.0/SiO_2$ and (**d**) $Ring\text{-}mSiO_2/Pt\text{-}5.0/SiO_2$. (**e**) The change of $d_{spacing}$ as the function of temperature. (**f**) The change of relative particle size as the function of temperature.

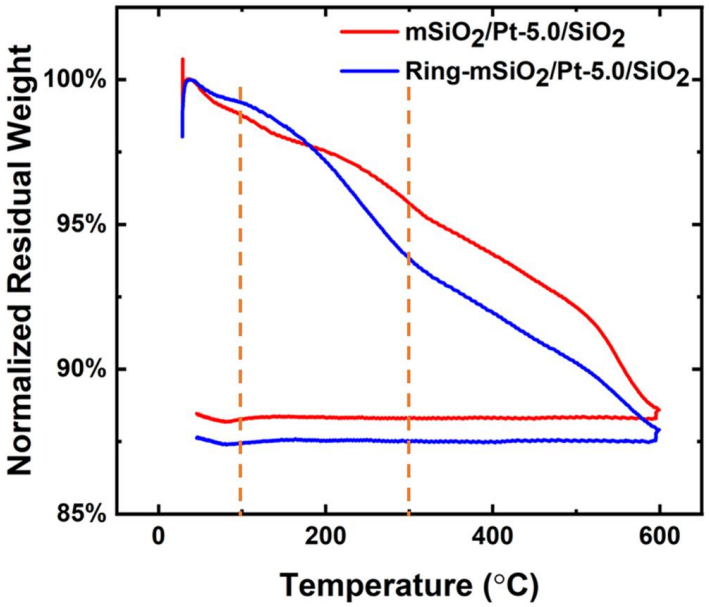

Figure 5. Thermogravimetric Analysis (TGA) analysis of $mSiO_2$/Pt-5.0/SiO_2 and Ring-$mSiO_2$/Pt-5.0/SiO_2.

3. Conclusions

We utilized several characterization methods to investigate two types of core-shell mesoporous silica nanoparticles with platinum nanoparticles loaded. Both mesoporous nanoparticles were synthesized successfully. The surface parameters were studied by the N_2 adsorption and desorption experiment. Surface area, pore size, and pore volume were determined. The structures of mesoporous nanoparticles were studied by synchrotron-based USAXS/SAXS, which demonstrated the size of the particles and the pores' diameter. The SAXS heating experiment and the TGA experiment were used to outline the thermal stabilities and the pyrolysis processes. High-resolution TEM was also deployed to understand the structure of both nanoparticles better. The core-shell structure, the mesopores of the shell, and the Pt nanoparticles can be observed. In addition to obtaining the detailed data, we have thus constructed a complete set of well-established characterization methods for mesoporous nanoparticles. We found that with these integrated methods, we were able to obtain detailed information about morphology and thermal stability of porous nanomaterial and thus distinguish similar nanomaterials. In future work, we plan to determine the role of the ring structure to see if it helps to accelerate or delay the catalyst process.

4. Materials and Methods

4.1. Chemicals and Materials

Cyclohexane (ACS grade), polyvinylpyrrolidone (PVP-K30, Mw = 40,000), Potassium tetrachloroplatinate (K_2PtCl_4, trace metal grade, 99.9%), Myristyltrimethylammonium bromide (C_{14}TAB, 99%), 3-aminopropyl trimethoxy silane (APTS, 97%), hexadecyltrimethylammonium bromide (C_{16}TAB, 98%), L-arginine (Reagent grade, ≥98%), and tetraethyl orthosilicate (TEOS, 98%) were purchased from Sigma-Aldrich (St. Louis, MO, USA). Ammonia hydroxide ($NH_3 \cdot H_2O$, 28–30%), hydrochloric acid (Reagent grade), Methanol (ACS grade), hexanes (HPLC grade), 2-propanol (ACS grade), acetone (ACS grade), and ethanol (200 proof) were purchased from Thermo Fischer Scientific (Waltham, MA, USA). Ethylene glycol (BDH, 99%) was purchased from VWR (Radnor, PA, USA). All chemicals were used as received unless otherwise notified. Ultrapure water was obtained from Milli-Q plus (Burlington, MA, USA).

4.2. Synthesis of $mSiO_2$/Pt-5.0/SiO_2 and Ring-$mSiO_2$/Pt-5.0/SiO_2

The synthesis process of $mSiO_2$/Pt-5.0/SiO_2 was reported in the previous article [26]. Simply put, the prepared Pt NPs were loaded on the NH_2-functionalized silica spheres, then a mesoporous SiO_2 shell was grown on the surface of the Pt NPs loaded SiO_2 spheres [26]. C_{16}TAB was used as the templating agent, and TEOS was used as the SiO_2 precursor [26]. The synthesis of Ring-$mSiO_2$/Pt-5.0/SiO_2 is similar to the synthesis of $mSiO_2$/Pt-5.0/SiO_2 with the difference in the silica precursor addition. After 30 min of gentle stirring with ammonia solution added, the mixture of 100 µL of TEOS with 700 µL of TEOS was added dropwise into the solution. After 40 min, a mixture of 20 µL APTS and 200 µL TEOS was added to the solution dropwise. Then after 40 min of gentle stirring, a solution of 600 µL TEOS in 4 mL ethanol was added in a dropwise manner in portions (3 × 200 µL) every 30 min to the above suspension. For both nanomaterials, after the last portion of the TEOS addition, the whole systems were left stirring for another 6 h hours to make sure the shell growth was finished. Then products were then isolated by centrifuge and washed with ethanol 3 times. The surfactants were removed by acid reflux. Typically, the washed product was redispersed into 15 mL of methanol and 1 mL of concentrate hydrochloric acid. Then it was refluxed at 80 °C for 24 h. The final product was recovered by centrifuge and washed with ethanol 5 times. Finally, the sample was vacuum-dried at room temperature. (In a typical synthesis, ~250 mg of catalyst can be obtained.)

4.3. Surface Area Analysis

N_2 adsorption and desorption isotherms were obtained on a Micromeritics 3Flex. The sample volume of 150 mg was outgassed under dynamic vacuum at 200 °C for 10 h. Surface areas were calculated using Brunauer–Emmett–Teller (BET) theory, and pore sizes were calculated with the Barrett–Joyner–Halenda (BJH) model. Nonlocal Density Function Theory (NLDFT) pore-size distribution was also obtained to compare the micropore range between samples.

4.4. Ultra Small-Angle X-Ray Scattering (USAXS)

USAXS/SAXS measurements were carried out at the sector 9-ID-C of the Advanced Photon Source at the Argonne National Laboratory [40]. The X-ray energy was 24 keV with exposure times of 5 min.

4.5. Transmission Electron Microscopy (TEM)

A JEM-2100F field emission electron microscope took TEM images at an acceleration voltage of 200 kV. Samples were prepared by dropping the silica nanoparticle suspension on 400 mesh carbon-coated copper grids and allowed to dry.

4.6. SAXS Heating Experiment

The SAXS heating experiments were performed at the 12-ID-B station at the Advanced Photon Source of the Argonne National Laboratory with an X-ray energy of 13.3 keV and exposure time of 0.2 s. The sample to detector distance (SDD) was 1999.78 mm. The heating ranges were from 30 °C to 400 °C.

4.7. Thermogravimetric Analysis (TGA)

A Mettler Toledo TGA SDTA851e took TGA information. The samples were heated up from 25 °C to 600 °C at the rate of 10 °C/min and maintained at 600 °C for 10 min in the nitrogen atmosphere. Before the heating program was initiated, we swapped the furnace with nitrogen to remove residual oxygen.

Author Contributions: Conceptualization, methodology, resources, funding acquisition, project administration, supervision, B.L., W.H. and T.L.; TEM, Y.L.; software, formal analysis, data curation, writing, X.L., X.W., B.L. and T.L. All authors have read and agreed to the published version of the manuscript.

Funding: This work was supported by the Institute for Cooperative Upcycling of Plastics (iCOUP), an En-ergy Frontier Research Center funded by the U.S. Department of Energy (DOE), Office of Basic Energy Sciences, Division of Chemical Sciences, Geosciences, and Biosciences, under Contract DE-AC-02-07CH11358 (Ames Laboratory) and DE-AC-02-06CH11357 (Argonne National Laboratory). Use of the Center for Nanoscale Materials, an Office of Science user facility, was supported by the U.S. Department of Energy, Office of Science, Office of Basic Energy Sciences, under Contract No. DE-AC02-06CH11357. This research used resources of the Advanced Photon Source, a U.S. Department of Energy (DOE) Office of Science User Facility operated for the DOE Office of Science by Argonne National Laboratory under Contract No. DE-AC02-06CH11357.

Data Availability Statement: Data can be obtained through contacting the authors.

Acknowledgments: We would like to acknowledge Xiao-min Lin from the Center for Nanoscale Materials, Argonne National Laboratory, for the help of TGA.

Conflicts of Interest: The authors declare no conflict of interest.

References

1. Li, W.C.; Tse, H.F.; Fok, L. Plastic waste in the marine environment: A review of sources, occurrence and effects. *Sci. Total Environ.* **2016**, *566–567*, 333–349. [CrossRef] [PubMed]
2. Liang, Y.; Tan, Q.; Song, Q.; Li, J. An analysis of the plastic waste trade and management in Asia. *Waste Manag.* **2021**, *119*, 242c253. [CrossRef] [PubMed]
3. Zhang, F.; Zhao, Y.; Wang, D.; Yan, M.; Zhang, J.; Zhang, P.; Ding, T.; Chen, L.; Chen, C. Current technologies for plastic waste treatment: A review. *J. Clean. Prod.* **2021**, *282*, 124523. [CrossRef]
4. Rochman, C.M.; Browne, M.A.; Halpern, B.S.; Hentschel, B.T.; Hoh, E.; Karapanagioti, H.K.; Rios-Mendoza, L.M.; Takada, H.; Teh, S.; Thompson, R.C. Classify plastic waste as hazardous. *Nature* **2013**, *494*, 169–171. [CrossRef]
5. Browne, M.A.; Dissanayake, A.; Galloway, T.S.; Lowe, D.M.; Thompson, R.C. Ingested Microscopic Plastic Translocates to the Circulatory System of the Mussel, *Mytilus edulis* (L.). *Environ. Sci. Technol.* **2008**, *42*, 5026–5031. [CrossRef] [PubMed]
6. Law, K.L.; Starr, N.; Siegler, T.R.; Jambeck, J.R.; Mallos, N.J.; Leonard, G.H. The United States's contribution of plastic waste to land and ocean. *Sci. Adv.* **2020**, *6*, eabd0288. [CrossRef]
7. Ellis, L.D.; Rorrer, N.A.; Sullivan, K.P.; Otto, M.; McGeehan, J.E.; Román-Leshkov, Y.; Wierckx, N.; Beckham, G.T. Chemical and biological catalysis for plastics recycling and upcycling. *Nat. Catal.* **2021**, *4*, 539–556. [CrossRef]
8. Jambeck Jenna, R.; Geyer, R.; Wilcox, C.; Siegler Theodore, R.; Perryman, M.; Andrady, A.; Narayan, R.; Law Kara, L. Plastic waste inputs from land into the ocean. *Science* **2015**, *347*, 768–771. [CrossRef]
9. Rahimi, A.; García, J.M. Chemical recycling of waste plastics for new materials production. *Nat. Rev. Chem.* **2017**, *1*, 0046. [CrossRef]
10. Jie, X.; Li, W.; Slocombe, D.; Gao, Y.; Banerjee, I.; Gonzalez-Cortes, S.; Yao, B.; AlMegren, H.; Alshihri, S.; Dilworth, J.; et al. Microwave-initiated catalytic deconstruction of plastic waste into hydrogen and high-value carbons. *Nat. Catal.* **2020**, *3*, 902–912. [CrossRef]
11. Saeaung, K.; Phusunti, N.; Phetwarotai, W.; Assabumrungrat, S.; Cheirsilp, B. Catalytic pyrolysis of petroleum-based and biodegradable plastic waste to obtain high-value chemicals. *Waste Manag.* **2021**, *127*, 101–111. [CrossRef]
12. Choi, J.; Yang, I.; Kim, S.S.; Cho, S.Y.; Lee, S. Upcycling Plastic Waste into High Value-Added Carbonaceous Materials. *Macromol. Rapid Commun.* **2021**, *43*, 2100467. [CrossRef] [PubMed]
13. Jia, X.; Qin, C.; Friedberger, T.; Guan, Z.; Huang, Z. Efficient and selective degradation of polyethylenes into liquid fuels and waxes under mild conditions. *Sci. Adv.* **2016**, *2*, e1501591. [CrossRef] [PubMed]
14. Okan, M.; Aydin, H.M.; Barsbay, M. Current approaches to waste polymer utilization and minimization: A review. *J. Chem. Technol. Biotechnol.* **2019**, *94*, 8–21. [CrossRef]
15. Borsodi, N.; Szentes, A.; Miskolczi, N.; Wu, C.; Liu, X. Carbon nanotubes synthetized from gaseous products of waste polymer pyrolysis and their application. *J. Anal. Appl. Pyrolysis* **2016**, *120*, 304–313. [CrossRef]
16. Rorrer, J.E.; Beckham, G.T.; Román-Leshkov, Y. Conversion of Polyolefin Waste to Liquid Alkanes with Ru-Based Catalysts under Mild Conditions. *JACS Au* **2021**, *1*, 8–12. [CrossRef] [PubMed]
17. Celik, G.; Kennedy, R.M.; Hackler, R.A.; Ferrandon, M.; Tennakoon, A.; Patnaik, S.; LaPointe, A.M.; Ammal, S.C.; Heyden, A.; Perras, F.A.; et al. Upcycling Single-Use Polyethylene into High-Quality Liquid Products. *ACS Cent. Sci.* **2019**, *5*, 1795–1803. [CrossRef]
18. Hackler, R.A.; Vyavhare, K.; Kennedy, R.M.; Celik, G.; Kanbur, U.; Griffin, P.J.; Sadow, A.D.; Zang, G.; Elgowainy, A.; Sun, P.; et al. Synthetic Lubricants Derived from Plastic Waste and their Tribological Performance. *ChemSusChem* **2021**, *14*, 4181–4189. [CrossRef]
19. Peczak, I.L.; Kennedy, R.M.; Hackler, R.A.; Wang, R.; Shin, Y.; Delferro, M.; Poeppelmeier, K.R. Scalable Synthesis of $Pt/SrTiO_3$ Hydrogenolysis Catalysts in Pursuit of Manufacturing-Relevant Waste Plastic Solutions. *ACS Appl. Mater. Interfaces* **2021**, *13*, 58691–58700. [CrossRef]

20. Lee, J.; Jackson, D.H.K.; Li, T.; Winans, R.E.; Dumesic, J.A.; Kuech, T.F.; Huber, G.W. Enhanced stability of cobalt catalysts by atomic layer deposition for aqueous-phase reactions. *Energy Environ. Sci.* **2014**, *7*, 1657–1660. [CrossRef]
21. Alba-Rubio, A.C.; O'Neill, B.J.; Shi, F.; Akatay, C.; Canlas, C.; Li, T.; Winans, R.; Elam, J.W.; Stach, E.A.; Voyles, P.M.; et al. Pore Structure and Bifunctional Catalyst Activity of Overlayers Applied by Atomic Layer Deposition on Copper Nanoparticles. *ACS Catal.* **2014**, *4*, 1554–1557. [CrossRef]
22. Lu, Z.; Tracy, R.W.; Abrams, M.L.; Nicholls, N.L.; Barger, P.T.; Li, T.; Stair, P.C.; Dameron, A.A.; Nicholas, C.P.; Marshall, C.L. Atomic Layer Deposition Overcoating Improves Catalyst Selectivity and Longevity in Propane Dehydrogenation. *ACS Catal.* **2020**, *10*, 13957–13967. [CrossRef]
23. Xiao, C.; Maligal-Ganesh, R.V.; Li, T.; Qi, Z.; Guo, Z.; Brashler, K.T.; Goes, S.; Li, X.; Goh, T.W.; Winans, R.E.; et al. High-Temperature-Stable and Regenerable Catalysts: Platinum Nanoparticles in Aligned Mesoporous Silica Wells. *ChemSusChem* **2013**, *6*, 1915–1922. [CrossRef] [PubMed]
24. Fang, X.; Liu, Z.; Hsieh, M.-F.; Chen, M.; Liu, P.; Chen, C.; Zheng, N. Hollow Mesoporous Aluminosilica Spheres with Perpendicular Pore Channels as Catalytic Nanoreactors. *ACS Nano* **2012**, *6*, 4434–4444. [CrossRef] [PubMed]
25. Maligal-Ganesh, R.V.; Pei, Y.; Xiao, C.; Chen, M.; Goh, T.W.; Sun, W.; Wu, J.; Huang, W. Sub-5 nm Intermetallic Nanoparticles Confined in Mesoporous Silica Wells for Selective Hydrogenation of Acetylene to Ethylene. *ChemCatChem* **2020**, *12*, 3022–3029. [CrossRef]
26. Tennakoon, A.; Wu, X.; Paterson, A.L.; Patnaik, S.; Pei, Y.; LaPointe, A.M.; Ammal, S.C.; Hackler, R.A.; Heyden, A.; Slowing, I.I.; et al. Catalytic upcycling of high-density polyethylene via a processive mechanism. *Nat. Catal.* **2020**, *3*, 893–901. [CrossRef]
27. Feng, Y.; Panwar, N.; Tng, D.J.H.; Tjin, S.C.; Wang, K.; Yong, K.-T. The application of mesoporous silica nanoparticle family in cancer theranostics. *Coord. Chem. Rev.* **2016**, *319*, 86–109. [CrossRef]
28. Alyassin, Y.; Sayed, E.G.; Mehta, P.; Ruparelia, K.; Arshad, M.S.; Rasekh, M.; Shepherd, J.; Kucuk, I.; Wilson, P.B.; Singh, N.; et al. Application of mesoporous silica nanoparticles as drug delivery carriers for chemotherapeutic agents. *Drug Discov. Today* **2020**, *25*, 1513–1520. [CrossRef]
29. Eivazzadeh-Keihan, R.; Chenab, K.K.; Taheri-Ledari, R.; Mosafer, J.; Hashemi, S.M.; Mokhtarzadeh, A.; Maleki, A.; Hamblin, M.R. Recent advances in the application of mesoporous silica-based nanomaterials for bone tissue engineering. *Mater. Sci. Eng. C* **2020**, *107*, 110267. [CrossRef]
30. Salmani, M.H.; Ehrampoush, M.H.; Eslami, H.; Eftekhar, B. Synthesis, characterization and application of mesoporous silica in removal of cobalt ions from contaminated water. *Groundw. Sustain. Dev.* **2020**, *11*, 100425. [CrossRef]
31. Dong, B.; Pei, Y.; Zhao, F.; Goh, T.W.; Qi, Z.; Xiao, C.; Chen, K.; Huang, W.; Fang, N. In situ quantitative single-molecule study of dynamic catalytic processes in nanoconfinement. *Nat. Catal.* **2018**, *1*, 135–140. [CrossRef]
32. Dong, B.; Pei, Y.; Mansour, N.; Lu, X.; Yang, K.; Huang, W.; Fang, N. Deciphering nanoconfinement effects on molecular orientation and reaction intermediate by single molecule imaging. *Nat. Commun.* **2019**, *10*, 4815. [CrossRef] [PubMed]
33. Dong, B.; Mansour, N.; Pei, Y.; Wang, Z.; Huang, T.; Filbrun, S.L.; Chen, M.; Cheng, X.; Pruski, M.; Huang, W.; et al. Single Molecule Investigation of Nanoconfinement Hydrophobicity in Heterogeneous Catalysis. *J. Am. Chem. Soc.* **2020**, *142*, 13305–13309. [CrossRef]
34. Li, T.; Senesi, A.J.; Lee, B. Small Angle X-ray Scattering for Nanoparticle Research. *Chem. Rev.* **2016**, *116*, 11128–11180. [CrossRef] [PubMed]
35. Li, T.; Karwal, S.; Aoun, B.; Zhao, H.; Ren, Y.; Canlas, C.P.; Elam, J.W.; Winans, R.E. Exploring Pore Formation of Atomic Layer-Deposited Overlayers by in Situ Small- and Wide-Angle X-ray Scattering. *Chem. Mater.* **2016**, *28*, 7082–7087. [CrossRef]
36. Schlumberger, C.; Scherdel, C.; Kriesten, M.; Leicht, P.; Keilbach, A.; Ehmann, H.; Kotnik, P.; Reichenauer, G.; Thommes, M. Reliable surface area determination of powders and meso/macroporous materials: Small-angle X-ray scattering and gas physisorption. *Microporous Mesoporous Mater.* **2022**, *329*, 111554. [CrossRef]
37. Liu, Y.; Paskevicius, M.; Sofianos, M.V.; Parkinson, G.; Wang, S.; Li, C.-Z. A SAXS study of the pore structure evolution in biochar during gasification in H_2O, CO_2 and H_2O/CO_2. *Fuel* **2021**, *292*, 120384. [CrossRef]
38. Li, T.; Zan, X.; Winans, R.E.; Wang, Q.; Lee, B. Biomolecular Assembly of Thermoresponsive Superlattices of the Tobacco Mosaic Virus with Large Tunable Interparticle Distances. *Angew. Chem. Int. Ed.* **2013**, *52*, 6638–6642. [CrossRef]
39. George, C.; Littlewood, P.; Stair, P.C. Understanding Pore Formation in ALD Alumina Overcoats. *ACS Appl. Mater. Interfaces* **2020**, *12*, 20331–20343. [CrossRef]
40. Ilavsky, J.; Zhang, F.; Allen, A.J.; Levine, L.E.; Jemian, P.R.; Long, G.G. Ultra-Small-Angle X-ray Scattering Instrument at the Advanced Photon Source: History, Recent Development, and Current Status. *Metall. Mater. Trans. A* **2013**, *44*, 68–76.